

Segmentation of MRI Images by Adaptive Degenerate Diffusion

Radek Mácá, Michal Beneš, and Jaroslav Tintěra

Abstract—This article presents the application of a segmentation algorithm based on numerical solution of a partial differential equation of the level set type with incorporated a priori knowledge of the processed data. The semi-implicit complementary-volume numerical scheme is used to derive the algorithm. In particular, we focus on the segmentation of the left heart ventricle from the cardiac MRI data. Using a suitable modification of the level set equation together with an image thresholding, the objects in the image such as the left ventricle or the papillary muscles can be detected. The purpose of the article is to indicate how the algorithm parameters are set up and how the a priori knowledge helps to getting satisfactory segmentation results.

Index Terms—image segmentation, partial differential equation, level set method, co-volume method, cardiac MRI

I. INTRODUCTION

IN the early years of the magnetic resonance imaging (MRI) in medicine, the heart was the most difficult organ to investigate. Over the last two decades MRI has evolved to become an important clinical imaging technique for heart and great vessels. Nowadays, imaging is an essential part of medical decision-making (see [1]). The presented work is motivated by the need of medical practice for automatic evaluation of the dynamical images of the heart obtained by cardiac MRI. A typical example could be an accurate measurement of the heart ventricle volume during the heart contraction showing the contractive ability of the myocardium. Within this framework, the main task is to find the region inside the ventricle which corresponds to the blood in the ventricle. We attempt to construct and tune a segmentation algorithm based on the numerical solution of a partial differential equation of the level set type. The algorithm is controlled by the gradient and intensity of MRI data in such a way that the edges of the objects can be found. More particularly, the algorithm is given by the numerical solution of the level set equation by the semi-implicit complementary-volume numerical scheme. The detailed description and mathematical analysis of this scheme can be found in [2], [3], [4], [5]. The main purpose of this article is to describe the segmentation algorithm, algorithm parameters and their adjustment used for segmentation of the left heart ventricle from the cardiac MRI images.

Manuscript received December 29, 2013; revised June 16, 2014. This work was supported by the grant of the Ministry of Education of the Czech Republic RVO – 68407700 and by the project “Advanced Supercomputing Methods for Implementation of Mathematical Models” of the Student Grant Agency of the Czech Technical University in Prague No. SGS11/161/OHK4/3T/14.

R. Mácá and M. Beneš are with the Department of Mathematics, Faculty of Nuclear Sciences and Physical Engineering, Czech Technical University in Prague, Czech Republic e-mail: radek.maca@fjfi.cvut.cz and michal.benes@fjfi.cvut.cz.

J. Tintěra is with the Institute of Clinical and Experimental Medicine, Prague, Czech Republic.

This paper presents the latest results of used method already published in [6]. Mainly, it introduces tailored parameters set-up to obtain best possible results on given set of MRI image data. The robustness and applicability of proposed segmentation algorithm is proven on wider set of MRI data series. Last but not least, an unique comparison study on fifteen different patients with rich variety of heart myocardium viability is introduced.

The main task of image segmentation is a partitioning the image plane into multiple segments (sets of pixels defining meaningful areas). Over the last few decades a large amount of segmentation algorithms have been proposed [7]. An enormous impact in the segmentation community had the Snakes approach introduced by Kass et al. in [8]. Afterwards, this approach were thoroughly studied, e.g. in [9], [10], [11], [12]. Among other approaches to the image segmentation we describe a given segment in the image as a hyperplane Γ , e.g. as a curve in the case of 2D images. There are two main description of Γ . First, the parametric approach can be used. It means that the curve is parameterized with respect to the curve parameter (see [13], [14]). Second, Γ is represented implicitly as the level line of some embedding function. The most popular method using implicit approach are the level set methods [15], [16], [17]. Last but not least the region based segmentation can be described using a statistical formulation [18], [19], [20], [21].

In the field of medical image processing we could mention approaches based on the diffusion driven segmentation. Broadly using models include so called level set equation which could be derived either from level set formulation [5], [17], [22] or from the geodesic active contours model [23], [24]. In (see [25], [26]) an algorithm using the phase-field approach to the mean curvature flow is presented. The segmentation model is given by the Allen-Cahn equation [27]. In [28], [29] the Allen-Cahn equation is used to segment the left heart ventricle volume and the wall of the left heart ventricle. A different method is based on the graph cuts [30], [31]. This method is based on the Ford-Fulkerson algorithm, which computes the maximum flow in a directed graph created from a given image. The latest result of this method can be found in [32] and [33].

Currently, the three-dimensional [2] and the four-dimensional (space and time) [4], [34], [35], [36] methods based on various other approaches became used in image segmentation. Recently, a priori information carried by the image data has been included into the segmentation models (see [37], [38], [39], [40]).

II. DEGENERATE DIFFUSION IN IMAGE PROCESSING

The segmentation of the left heart ventricle volume is the important part of the cardiac MRI data postprocessing.

Examination of the heart ventricle consists of several hundreds of MR images covering the entire left ventricle volume and recording complete cardiac-cycle interval with a given temporal resolution. As discussed in [28], the current level of the MRI acquisition allows to get a relatively low number of 2D slices along the main heart axis through the cardiac cycle, provided a reasonable quality of the images is maintained. This is the reason why we consider segmentation of 2D slices instead of fully 3D segmentation in this text.

In our case, the MRI images are segmented separately each of other by means of the curve $\Gamma(t) \subset \Omega$ in \mathbb{R}^2 propagating in the normal direction with velocity V . The velocity V at a curve point $x \in \Gamma(t)$ is given by its (mean) curvature κ_Γ and external force F as follows

$$V = -\kappa_\Gamma + F. \tag{1}$$

For the segmentation purposes, law (1) can be modified by incorporating the influence of the processed signal (or its gradient) into the curvature and the force terms. The motion law (1) can be treated by the level set method. In this case, $\Gamma(t)$ is represented as a level set

$$\Gamma(t) = \{x \in \Omega \mid u(t, x) = 0\}, \tag{2}$$

where $u : [0, T] \times \Omega \rightarrow \mathbb{R}$.

The evolution equation implicitly describing the motion of $\Gamma(t)$ given by (2) with velocity V in the outward normal direction is derived as follows.

Using the sign convention we can express the normal vector, the normal velocity and the mean curvature as

$$\vec{n} = \frac{\nabla u}{|\nabla u|}, \quad V = -\frac{\partial_t u}{|\nabla u|}, \quad \kappa_\Gamma = \nabla \cdot \vec{n} = \nabla \cdot \frac{\nabla u}{|\nabla u|}. \tag{3}$$

Substituting (3) to equation (1), we obtain the level set equation in the form

$$\partial_t u = |\nabla u| \nabla \cdot \frac{\nabla u}{|\nabla u|} - |\nabla u| F, \tag{4}$$

where we denote $\partial_t u := \partial u / \partial t$. This equation has been extensively studied and applied (see [15], [16], [17]). This experience suggests a regularization proposed by Evans and Spruck (see [15]) which is useful both for theory and numerical computation in the form:

$$\partial_t u = |\nabla u|_\varepsilon \nabla \cdot \frac{\nabla u}{|\nabla u|_\varepsilon} - |\nabla u|_\varepsilon F, \tag{5}$$

where

$$|\nabla u|_\varepsilon = \sqrt{\varepsilon^2 + |\nabla u|^2}, \quad \varepsilon > 0. \tag{6}$$

The known features of the level set equation based mainly on the controlled motion of isolines of the solution naturally led to its use in the image processing (see [5], [17], [22], [23], [24]).

In particular, the detection of image object edges is a one of tasks in image segmentation. Edges in the input image $I^0 : \Omega \rightarrow \{0, 1, 2, \dots, I_{\max}\}$ (represented by the matrix $n_{x_1} \times n_{x_2}$, where $\Omega = (0, n_{x_1} / \max\{n_{x_1}, n_{x_2}\}) \times (0, n_{x_2} / \max\{n_{x_1}, n_{x_2}\})$) can be recognized by the magnitude of its spatial gradient. The level set equation operating in Ω can be modified as follows

$$\begin{aligned} \partial_t u = & |\nabla u|_\varepsilon \nabla \cdot \left(g(|I^0 * \nabla G_\sigma|) \frac{\nabla u}{|\nabla u|_\varepsilon} \right) \\ & - g(|I^0 * \nabla G_\sigma|) |\nabla u|_\varepsilon F, \end{aligned} \tag{7}$$

where $g : \mathbb{R}_0^+ \rightarrow \mathbb{R}^+$ is a non-increasing function for which $g(0) = 1$ and $g(s) \rightarrow 0$ for $s \rightarrow +\infty$. This function was first used by P. Perona and J. Malik ([41] in 1987) to modify the heat equation into a nonlinear diffusion equation which maintains edges in an image. Consequently, the function g is called the Perona-Malik function. We put $g(s) = 1/(1 + \lambda s^2)$ with $\lambda \geq 0$. $G_\sigma \in \mathcal{C}^\infty(\mathbb{R}^2)$ is a smoothing kernel, e.g. the Gauss function with zero mean and variance σ^2

$$G_\sigma(x) = \frac{1}{\sqrt{2\pi\sigma^2}} e^{-\frac{|x|^2}{2\sigma^2}}, \tag{8}$$

which is used to pre-smoothing (denoising) of image gradients by convolution

$$(I^0 * \nabla G_\sigma)(x) = \int_{\mathbb{R}^2} \bar{I}^0(x - y) \nabla G_\sigma(y) dy, \tag{9}$$

where \bar{I}^0 is the extension of I^0 to \mathbb{R}^2 by, e.g., mirroring, periodic prolongation or zero padding. Let us note that equation (7) can be rewritten into the advection-diffusion form

$$\partial_t u = \underbrace{g^0 |\nabla u|_\varepsilon \nabla \cdot \left(\frac{\nabla u}{|\nabla u|_\varepsilon} \right)}_{(D)} + \underbrace{\nabla g^0 \cdot \nabla u}_{(A)} - \underbrace{g^0 |\nabla u|_\varepsilon F}_{(F)}. \tag{10}$$

For convenience, the abbreviation $g^0 = g(|I^0 * \nabla G_\sigma|)$ is used. (D) in (10) denotes the diffusion term, (A) the advection term and (F) the external force term. The term g^0 is called the edge detector which is approximately equal to zero close to image edges. Consequently, the evolution of the segmentation function slows down in the neighbourhood of image edges. On the contrary, in parts of the image with constant intensity the edge detector equals one. The advection term attracts the segmentation function to the image edges. We propose an advection parameter \mathcal{A} to change the magnitude of the advection term and to obtain the modified level set equation, namely

$$\partial_t u = g^0 |\nabla u|_\varepsilon \nabla \cdot \left(\frac{\nabla u}{|\nabla u|_\varepsilon} \right) + \mathcal{A} \nabla g^0 \cdot \nabla u - g^0 |\nabla u|_\varepsilon F. \tag{11}$$

A. Initial-boundary value problem

As a parabolic partial differential equation, (11) requires initial and boundary conditions. For this purpose, we define the signed distance function (SDF).

Let Γ_{in} be the interior of $\Gamma(t)$ and Γ_{out} be the exterior of $\Gamma(t)$. Consequently $\Gamma = \partial\Gamma_{\text{in}} = \partial\Gamma_{\text{out}}$, $\Gamma_{\text{in}} \cup \Gamma \cup \Gamma_{\text{out}} = \Omega$ at any time. Then the signed distance function (d_Γ) is given by

$$d_\Gamma(t, x) = \begin{cases} \text{dist}(x, \Gamma(t)) & x \in \Gamma_{\text{out}}, \\ 0 & x \in \Gamma(t), \\ -\text{dist}(x, \Gamma(t)) & x \in \Gamma_{\text{in}}, \end{cases} \tag{12}$$

where $\text{dist}(x, \Gamma(t)) = \min\{|x - y| \mid y \in \Gamma(t)\}$.

The initial curve Γ_0 as the initial guess has to be placed inside the segmentation object – the left heart ventricle. To expand the initial curve, velocity (1) has to be positive. Positive value of V implies that the external force satisfies the following inequality $F > \kappa_\Gamma$. The signed distance function (SDF) can be used as the initial condition for (11). At the beginning of the segmentation process for a given patient, i.e. for the first image, we have to place the initial curve Γ_0 into the left heart ventricle manually, e.g., as a circle. By

means of image segmentation, the initial curve Γ_0 is called the initial segmentation curve.

For a given Γ_0 we construct SDF d_{Γ_0} and set the initial condition as $u_{ini} = d_{\Gamma_0}$ referred to as the initial segmentation function. The definition (12) implies that the segmentation curve $\Gamma(t)$ is the zero level set of the segmentation function $u(t, x)$ for any $t \in [0, T]$.

The segmentation function u evolves from the initial segmentation function (Figure 1a) according to (11). This evolution distorts the original shape of u_{ini} into $u(t, x)$ which fails to have the unit gradient slopes (Figure 1b). At the beginning of next image segmentation it is convenient to use the result of the previous image segmentation $\Gamma(t) = \{x \in \mathbb{R}^2 \mid u(t, x) = 0\}$ and its signed distance function d_{Γ_t} as a new initial condition, i.e. as a new initial segmentation function. In this paper we use following notation:

- $u(t, x)$ is the segmentation function
- $u(0, x)$ is the initial segmentation function (SDF shape)
- $\Gamma(t)$ is the segmentation curve ($u(t, \Gamma(t)) = 0$)
- $\Gamma(0)$ is the initial segmentation curve ($u(0, \Gamma(0)) = 0$)

This is performed by means of the fast sweeping method introduced in [42]. This method is used to compute the viscosity solution of the following problem

$$\begin{aligned} |\nabla u(x)| &= 1 & x \in \Omega, \\ u(x) &= 0 & x \in \Gamma \subset \Omega. \end{aligned}$$

An example of a restored signed distance function is shown in Figure 1c.

Finally, using the zero Neumann boundary condition we define the following initial-boundary value problem

$$\begin{aligned} \partial_t u(t, x) &= g^0 |\nabla u|_{\varepsilon} \nabla \cdot \left(\frac{\nabla u}{|\nabla u|_{\varepsilon}} \right) \\ &\quad + \mathcal{A} \nabla g^0 \cdot \nabla u - g^0 |\nabla u|_{\varepsilon} F & \text{in } (0, T) \times \Omega, \\ \frac{\partial u}{\partial n}(t, x) &= 0 & \text{on } (0, T) \times \partial\Omega, \\ u(0, x) &= d_{\Gamma_0}(x) & \text{in } \Omega. \end{aligned}$$

Numerical algorithm solving this problem is the key part of the segmentation algorithm.

B. Related approaches

The motion of the segmentation level curves by (11) has several alternatives.

For example, the segmentation curve can be described directly, i.e. parametrically. Using a smooth time-dependent vector function

$$\vec{X} : I \times S \rightarrow \mathbb{R}^2,$$

where $S = (0, 1)$ is a fixed interval for curve parameter and $I = \langle 0, T \rangle$ is the time interval, the segmentation curve $\Gamma(t)$ is given as

$$\Gamma(t) = \{\vec{X}(t, v) \mid v \in S\}. \tag{13}$$

According to [43], the normal vector, the normal velocity and the curvature are expressed as follows

$$\vec{n} = \frac{\partial_v \vec{X}^\perp}{|\partial_v \vec{X}|}, \quad V = \partial_t \vec{X} \cdot \vec{n}, \quad \kappa_\Gamma = -\vec{n} \cdot \frac{\partial_{vv} \vec{X}}{|\partial_v \vec{X}|^2}. \tag{14}$$

Substitution into (1) yields the evolution law for $\vec{X} = \vec{X}(t, v)$ in the vectorial form of

$$\partial_t \vec{X} = \frac{\partial_{vv} \vec{X}}{|\partial_v \vec{X}|^2} + F \frac{\partial_v \vec{X}}{|\partial_v \vec{X}|}. \tag{15}$$

A modification containing the Perona-Malik function g^0

$$\partial_t \vec{X} = g^0 \frac{\partial_{vv} \vec{X}}{|\partial_v \vec{X}|^2} - \nabla g^0 + g^0 F \frac{\partial_v \vec{X}}{|\partial_v \vec{X}|} \tag{16}$$

endowed with the initial conditions

$$\vec{X}|_{t=0} = \vec{X}_0 \tag{17}$$

and with the periodic boundary conditions can serve in the segmentation of the image data as shown in [43].

Another variant is based on the phase-field approach to the mean curvature flow (see e.g. [26]). The function $p(t, x)$ evolves according to the following initial-boundary-value problem for the modified Allen-Cahn equation (see [27]):

$$\begin{aligned} \xi \frac{\partial p}{\partial t}(t, x) &= \xi \nabla \cdot (g^0 \nabla p) \\ &\quad + g^0 \left(\frac{1}{\xi} f_0(p) + \xi F |\nabla p| \right) & \text{in } (0, T) \times \Omega, \\ \frac{\partial p}{\partial n}(t, x) &= 0 & \text{on } (0, T) \times \partial\Omega, \\ p(0, x) &= p_{ini} & \text{in } \Omega. \end{aligned}$$

The function $p(t, x)$ has its values in $\langle 0, 1 \rangle$ which is guaranteed by the particular form of the polynomial function f_0 having the values of 0 and 1 as roots. The segmentation curve at time t is given by the level set

$$\Gamma(t) = \{x \in \Omega \mid p(t, x) = \frac{1}{2}\}.$$

The thickness of the transition layer between the values of $p = 0$ and $p = 1$ is given by the small parameter $0 < \xi \ll 1$. The profile of p across $\Gamma(t)$ remains stable for all t . When $\xi \rightarrow 0_+$ and $g(x) = 1$ the segmentation curve $\Gamma(t)$ evolves according to the mean-curvature evolution law (1). The application in MRI data segmentation can be found in [29].

All of these approaches related to the image segmentation should be generalized in the following manner. In variational point of view, one computes segmentation of a given image I^0 by evolving a curve (hypersurface) Γ in the direction of negative energy gradient with respect to the appropriate partial differential equations. The well-known approach called Snakes introduced by Kass in [8] evolves a curve (13) by locally minimizing the functional

$$E(\Gamma) = - \int |\nabla I^0(\Gamma)|^2 dv + \lambda_1 \int |\Gamma_v|^2 dv + \lambda_2 \int |\Gamma_{vv}|^2 dv, \tag{18}$$

where Γ_v and Γ_{vv} denote the first and second derivative with respect to the curve parameter v . The first term in (18) is the external energy influencing the model by the image information. The last two terms can be interpreted as an internal energy of the curve. Usually the term weighted by parameter λ_2 is not particularly important and therefore it is omitted in many related publications. In general, the idea of introducing the functional (18) goes through many image processing publications. The major difference between them is that some start from an energy concept, while others

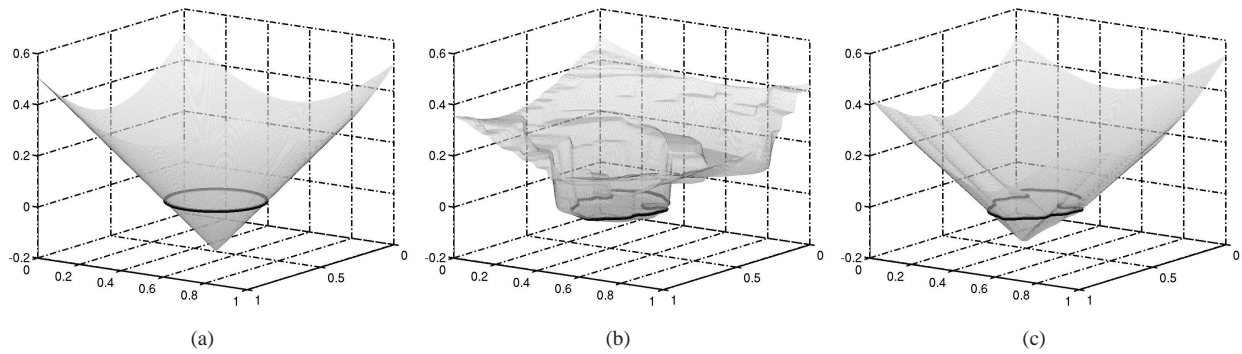


Fig. 1: Example of segmentation function. Initial segmentation function u_0 (a), segmentation function u for $(t > 0)$ (b), restored SDF (c). The graphs contain corresponding zero level line.

formulate directly their problem, e.g. in terms of level sets as we did in Section II.

III. SEGMENTATION ALGORITHM

A numerical scheme with justified key features such as stability and convergence can become a basis for a reliable and efficient algorithm. For this purpose, a semi-implicit co-volume space discretization is used. This approach is similar to [2], [3], [5], [44]. We choose a uniform discrete time step τ and approximate the time derivative in (11) by backward difference. The linear terms of the equation are approximated at the current time level while the nonlinear terms (i.e. $|\nabla u|_\varepsilon$) are treated at the previous time level. In this way we obtain the following semi-implicit discretization

$$\frac{u^k - u^{k-1}}{\tau} = g^0 |\nabla u^{k-1}|_\varepsilon \nabla \cdot \left(\frac{\nabla u^k}{|\nabla u^{k-1}|_\varepsilon} \right) + \mathcal{A} \nabla g^0 \cdot \nabla u^k - g^0 |\nabla u^{k-1}|_\varepsilon F. \quad (19)$$

To simplify the construction of spatial discretization, we rewrite the previous equation using the following expression

$$g^0 \nabla \cdot \left(\frac{\nabla u^k}{|\nabla u^{k-1}|_\varepsilon} \right) = \nabla \cdot \left(g^0 \frac{\nabla u^k}{|\nabla u^{k-1}|_\varepsilon} \right) - \nabla g^0 \cdot \frac{\nabla u^k}{|\nabla u^{k-1}|_\varepsilon}. \quad (20)$$

Next, we substitute (20) to (19). Dividing by $|\nabla u^{k-1}|_\varepsilon$, we get new form of (19)

$$\frac{1}{|\nabla u^{k-1}|_\varepsilon} \frac{u^k - u^{k-1}}{\tau} = \nabla \cdot \left(g^0 \frac{\nabla u^k}{|\nabla u^{k-1}|_\varepsilon} \right) + (\mathcal{A} - 1) \frac{1}{|\nabla u^{k-1}|_\varepsilon} \nabla g^0 \cdot \nabla u^k - g^0 F. \quad (21)$$

The co-volume method is used to construct a fully-discrete system of equations. The digital image is recorded on a structure of pixels with the rectangular shape. Each pixel includes the values of I^0 influencing the segmentation model. We relate the spatial approximations of the segmentation function u to the centers of image pixels. We evaluate the gradient of the segmentation function at the previous time step ($|\nabla u^{k-1}|_\varepsilon$) in (21). We put a triangulation inside the pixel structure and use the piecewise linear approximation of the segmentation function on this triangulation. This approach provides constant values of gradient on each triangle. For a

given pixel structure we build a triangulation in such a way that the centers of pixels are connected by new rectangular mesh. Each new rectangle is divided into four triangles of equal size. The pixel centers will be called the degree-of-freedom (DF) nodes. Other nodes will be called the non-degree-of-freedom (NDF) nodes. Let a function u be given by discrete values at DF nodes and u_h be a piecewise linear approximation of u on the triangulation. The value u_h at NDF nodes is given by the average value of the neighboring DF nodal values.

For triangulation \mathcal{T}_h given by the previous construction, we construct a co-volume (dual) mesh consisting of the cells p associated with DF nodes p of \mathcal{T}_h only. Without any confusion, we denote each co-volume and the corresponding DF node by the same symbol. In order to derive the co-volume spatial discretization the notation in Table I is introduced.

TABLE I: Co-volume notations.

C_p	...	set of all DF nodes q connected to the node p by an edge
σ_{pq}	...	edge connecting DF nodes p and q
h_{pq}	...	length of σ_{pq}
e_{pq}	...	common edge of co-volumes p and q ($\partial p = \bigcup_{q \in C_p} e_{pq}$)
\mathcal{E}_{pq}	...	set of triangles including the edge σ_{pq}
c_{pq}^T	...	length of the portion of e_{pq} that is in $T \in \mathcal{T}_h$ ($c_{pq}^T = e_{pq}^T \cap T $)
\mathcal{N}_p	...	set of $T \in \mathcal{T}_h$ including the vertex p
$ \nabla u_T $...	value of $ \nabla u_h $ on $T \in \mathcal{T}_h$
u_p	...	value of $u_h(x_p)$, where x_p is the coordinate of the node p on \mathcal{T}_h
u_{pq}	...	value of $u_h(x_{\frac{pq}{2}})$, where $x_{\frac{pq}{2}} = \sigma_{pq} \cap e_{pq}$
ν_p	...	outer normal of co-volume p
ν_{pq}	...	outer normal of co-volume p on e_{pq}

We integrate (21) over each co-volume p , $p = 1, \dots, M$ (M denotes the number of all DF nodes). The approximation of the left-hand side and the first term on the right-hand side of (21) can be found in [5]. Hence we provide the result of the approximation of these two terms without explanation. The left-hand side of (21) is approximated by

$$\int_p \frac{1}{|\nabla u^{k-1}|_\varepsilon} \frac{u^k - u^{k-1}}{\tau} dx \approx m(p) M_p^{k-1} \frac{u_p^k - u_p^{k-1}}{\tau}, \quad (22)$$

where $m(p)$ is the measure of co-volume p in \mathbb{R}^2 and M_p^{k-1}

is given by

$$M_p^{k-1} = \frac{1}{|\nabla u_p^{k-1}|_\varepsilon}, |\nabla u_p^{k-1}|_\varepsilon = \sum_{T \in \mathcal{N}_p} \frac{m(T \cap p)}{m(p)} |\nabla u_T^{k-1}|_\varepsilon,$$

where $T \cap p$ is the intersection of triangle T and co-volume p . In our case for $T \in \mathcal{N}_p$, it holds $m(T \cap p)/m(p) = 1/8$. Denoting the spatial step of the co-volume mesh by h we get $m(p) = h^2$. The approximation of the first term on the right-hand side of (21) is done using the divergence theorem

$$\begin{aligned} & \int_p \nabla \cdot \left(g^0 \frac{\nabla u^k}{|\nabla u^{k-1}|_\varepsilon} \right) dx \\ & \approx \sum_{q \in C_p} \left(\sum_{T \in \mathcal{E}_{pq}} c_{pq}^T \frac{g_T^0}{|\nabla u_T^{k-1}|_\varepsilon} \right) \frac{u_q^k - u_p^k}{h_{pq}}, \end{aligned} \tag{23}$$

where g_T^0 denotes approximation of g^0 on a triangle $T \in \mathcal{T}_h$. The advection term on the right-hand side of (21) is approximated by the first-order upwind scheme. We use the following approximation

$$\begin{aligned} & \int_p (\mathcal{A} - 1) \frac{1}{|\nabla u^{k-1}|_\varepsilon} \nabla g^0 \cdot \nabla u^k dx \\ & \approx (\mathcal{A}_p - 1) M_p^{k-1} \int_p \nabla g^0 \cdot \nabla u^k dx. \end{aligned}$$

Now we rewrite the scalar product of ∇g^0 and ∇u^k into the form

$$\nabla g^0 \cdot \nabla u^k = \nabla \cdot (\nabla g^0 u^k) - \Delta g^0 u^k.$$

Then we get

$$\int_p \nabla g^0 \cdot \nabla u^k dx = \int_p \nabla \cdot (\nabla g^0 u^k) dx - \int_p \Delta g^0 u^k dx. \tag{24}$$

The first term on the right hand side of (24) is approximated as follows

$$\int_p \nabla \cdot (\nabla g^0 u^k) dx = \int_{\partial p} \frac{\partial g^0}{\partial \nu_p} u^k ds \approx \sum_{q \in C_p} |e_{pq}| \frac{\partial g^0}{\partial \nu_{pq}} u_{pq}^k. \tag{25}$$

For the second term on the right hand side of (24) the divergence theorem implies

$$\begin{aligned} \int_p \Delta g^0 u^k dx & \approx u_p^k \int_p \Delta g^0 dx = u_p^k \int_{\partial p} \frac{\partial g^0}{\partial \nu_p} ds \\ & \approx u_p^k \sum_{q \in C_p} \int_{e_{pq}} \frac{\partial g^0}{\partial \nu_{pq}} ds \approx u_p^k \sum_{q \in C_p} |e_{pq}| \frac{\partial g^0}{\partial \nu_{pq}}. \end{aligned} \tag{26}$$

Then we can substitute (25) and (26) into (24) to get

$$\int_p \nabla g^0 \cdot \nabla u^k dx \approx \sum_{q \in C_p} |e_{pq}| \frac{\partial g^0}{\partial \nu_{pq}} (u_{pq}^k - u_p^k).$$

The approximation of the advection term is completed by the evaluation of u_{pq}^k . As mentioned above, we use the first-order upwind scheme

$$u_{pq}^k := \begin{cases} u_p^k & \text{for } \frac{\partial g^0}{\partial \nu_{pq}} > 0 \\ u_q^k & \text{for } \frac{\partial g^0}{\partial \nu_{pq}} < 0 \end{cases}.$$

Finally the above expressions are put together to get spatial approximation of the advection term

$$\begin{aligned} & \int_p (\mathcal{A} - 1) \frac{1}{|\nabla u^{k-1}|_\varepsilon} \nabla g^0 \cdot \nabla u^k dx \\ & \approx (\mathcal{A}_p - 1) M_p^{k-1} \sum_{q \in C_p} |e_{pq}| \min \left(\frac{\partial g^0}{\partial \nu_{pq}}, 0 \right) (u_q^k - u_p^k). \end{aligned} \tag{27}$$

The force term on the right-hand side of (24) is approximated as follows

$$\int_p g^0 F dx \approx m(p) g_p^0 F_p, \tag{28}$$

where g_p^0 denotes approximation of g^0 on the co-volume p . Using the notation

$$a_{pq}^{k-1} = \frac{1}{h_{pq}} \sum_{T \in \mathcal{E}_{pq}} c_{pq}^T \frac{g_T^0}{|\nabla u_T^{k-1}|_\varepsilon}, g_{pq} = |e_{pq}| \min \left(\frac{\partial g^0}{\partial \nu_{pq}}, 0 \right) \tag{29}$$

together with (22), (23), (27) and (28), the fully-discrete semi-implicit co-volume scheme is obtained

$$\begin{aligned} & \left[m(p) M_p^{k-1} + \tau \sum_{q \in C_p} (a_{pq}^{k-1} + (\mathcal{A}_p - 1) M_p^{k-1} g_{pq}) \right] u_p^k \\ & - \tau \sum_{q \in C_p} (a_{pq}^{k-1} + (\mathcal{A}_p - 1) M_p^{k-1} g_{pq}) u_q^k \\ & = m(p) M_p^{k-1} u_q^{k-1} - m(p) g_p^0 F_p. \end{aligned} \tag{30}$$

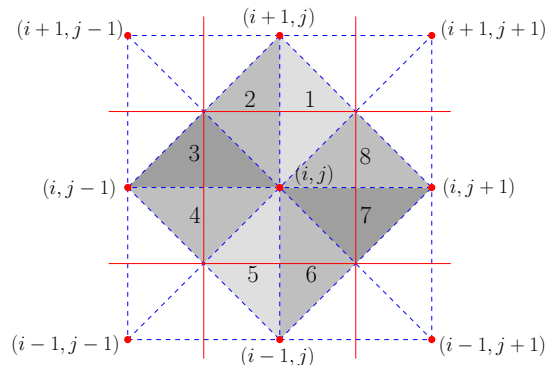


Fig. 2: Co-volume p associated with a couple (i, j) and set of 8 triangles $\mathcal{N}_{i,j}$ denoted by numbers 1 to 8.

For simplicity of the implementation we write the co-volume scheme using the structured notation common in finite difference methods. Let I^0 be the input image whose size is $n_{x_1} \times n_{x_2}$ where n_{x_1} represents number of pixels in the horizontal direction and n_{x_2} in the vertical direction. We associate the co-volume p and its corresponding DF node with a couple (i, j) , where $i \in \{1, \dots, n_{x_2}\}$, $j \in \{1, \dots, n_{x_1}\}$. Using this notation, the unknown value u_p^k is associated with $u_{i,j}^k$ and \mathcal{N}_p with $\mathcal{N}_{i,j}$. As we can see from the coefficient (29), we need to evaluate the absolute value of the gradient on each triangle from the set $\mathcal{N}_{i,j}$ (see Figure 2) denoted by $G_{i,j}^n$, $n \in \{1, \dots, 8\}$ at each discrete time step $k \in \{1, \dots, s\}$ and for every $i \in \{2, \dots, n_{x_2} - 1\}$, $j \in \{2, \dots, n_{x_1} - 1\}$ (except boundary pixels). For this purpose, we use the following expression exploring the discrete values of u^{k-1} , i.e. from the previous time step.

For example, $G_{i,j}^1$ is in the form

$$|G_{i,j}^1|^2 = \left(\frac{u_{i,j+1}^{k-1} + u_{i+1,j+1}^{k-1} - u_{i,j}^{k-1} - u_{i+1,j}^{k-1}}{2h} \right)^2 + \left(\frac{u_{i+1,j}^{k-1} - u_{i,j}^{k-1}}{h} \right)^2. \quad (31)$$

Other gradient discretization $G_{i,j}^2, \dots, G_{i,j}^8$ can be found in [5]. In the same way, but at the start-up of the algorithm only, we compute values $G_{i,j}^{\sigma,n}$, $n \in 1, \dots, 8$ replacing u^{k-1} by $I^{0,\sigma} := I^0 * G_\sigma$ in the above expressions, e.g.

$$|G_{i,j}^{\sigma,1}|^2 = \left(\frac{I_{i,j+1}^{0,\sigma} + I_{i+1,j+1}^{0,\sigma} - I_{i,j}^{0,\sigma} - I_{i+1,j}^{0,\sigma}}{2h} \right)^2 + \left(\frac{I_{i+1,j}^{0,\sigma} - I_{i,j}^{0,\sigma}}{h} \right)^2.$$

The convolution $I^0 * G_\sigma$ can be evaluated numerically as the solution of the linear heat equation at the time $t = \sigma^2/2$ with initial condition given by I^0 . For each $i \in \{2, \dots, n_{x_2} - 1\}$, $j \in \{2, \dots, n_{x_1} - 1\}$ we calculate the north, west, south and east coefficients

$$n_{ij} = \tau \frac{1}{2} \sum_{n=1}^2 \frac{g(G_{i,j}^{\sigma,n})}{\sqrt{\varepsilon^2 + (G_{i,j}^n)^2}} + \tau h (A_{i,j} - 1) m_{i,j} \min \left(\frac{g(G_{i+1,j}^\sigma) - g(G_{i,j}^\sigma)}{h}, 0 \right),$$

$$w_{ij} = \tau \frac{1}{2} \sum_{n=3}^4 \frac{g(G_{i,j}^{\sigma,n})}{\sqrt{\varepsilon^2 + (G_{i,j}^n)^2}} + \tau h (A_{i,j} - 1) m_{i,j} \min \left(\frac{g(G_{i,j-1}^\sigma) - g(G_{i,j}^\sigma)}{h}, 0 \right),$$

$$s_{ij} = \tau \frac{1}{2} \sum_{n=5}^6 \frac{g(G_{i,j}^{\sigma,n})}{\sqrt{\varepsilon^2 + (G_{i,j}^n)^2}} + \tau h (A_{i,j} - 1) m_{i,j} \min \left(\frac{g(G_{i-1,j}^\sigma) - g(G_{i,j}^\sigma)}{h}, 0 \right),$$

$$e_{ij} = \tau \frac{1}{2} \sum_{n=7}^8 \frac{g(G_{i,j}^{\sigma,n})}{\sqrt{\varepsilon^2 + (G_{i,j}^n)^2}} + \tau h (A_{i,j} - 1) m_{i,j} \min \left(\frac{g(G_{i,j+1}^\sigma) - g(G_{i,j}^\sigma)}{h}, 0 \right),$$

where $m_{i,j}$ denotes the following expression

$$m_{i,j} = \frac{1}{\sqrt{\varepsilon^2 + \left(\frac{1}{8} \sum_{n=1}^8 G_{i,j}^{\sigma,n} \right)^2}}.$$

If we define the diagonal coefficients by

$$c_{i,j} = n_{i,j} + w_{i,j} + s_{i,j} + e_{i,j} + m_{i,j} h^2$$

and the right hand sides at the k -th discrete time step by

$$r_{ij} = m_{i,j} h^2 u_{i,j}^{k-1} - \tau h^2 G_{i,j}^\sigma F_{i,j},$$

we get

$$c_{i,j} u_{i,j}^k - n_{i,j} u_{i+1,j}^k - w_{i,j} u_{i,j-1}^k - s_{i,j} u_{i-1,j}^k - e_{i,j} u_{i,j+1}^k = r_{i,j}. \quad (32)$$

Collecting these equations for inner DF nodes with the Neumann boundary condition we get a linear system to be solved. For this purpose the SOR (Successive Over-Relaxation) iterative method is used.

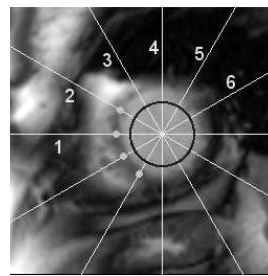
IV. DATA PREPROCESSING

In the cardiac MR images obtained by means of the bright blood technique (see [1], chapter 4), the blood in the ventricle is lighter than the myocardium and the surrounding tissue. It means that the blood in the ventricle has higher intensity than surrounding cardiac muscle. Using this information we can try to set a threshold I_{in} for picture elements surely inside the ventricle and a threshold I_{out} for picture elements surely in the myocardium and the surrounding tissue. These thresholds are set automatically using the following algorithm.

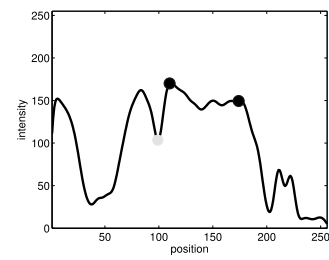
At the beginning of each image segmentation, i.e. for a given image and initial segmentation curve (ISC), we determine several lines (slices) passing through the point with minimum value of corresponding initial segmentation function having a shape of SDF. The slice configuration can be seen in Figure 3a. Then we plot the graphs of image intensities along these lines. The graphs for slice 1 and 6 are plotted in Figures 3b and 3d. In these graphs we find the local minima satisfying the following conditions:

- 1) The minimum does not lie inside the ISC
- 2) The minimum lies close to the intersection of ISC and the given slice (black points in Figure 3)
- 3) The minimum is less than the median (I_{med}) of image intensities inside the ISC
- 4) The closest maximum (which is further from the ISC is greater than $0.7I_{med}$ and the difference between this maximum and corresponding minimum is greater than $0.02I_{max}$

These conditions are designed in accordance with the bright blood data type, the heart anatomy, the position of initial segmentation curve and experimental computations. Finally, we set the threshold I_{out} as the maximal value from the minima satisfying conditions given above (grey points in Figure 3). The threshold I_{in} is set to I_{med} .



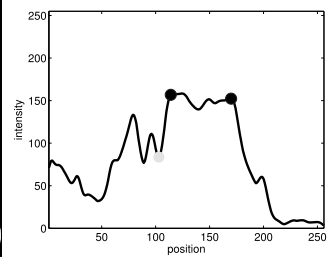
(a) Slices for given initial segmentation curve.



(b) Image intensities along slice 1.



(c) Image thresholding result.



(d) Image intensities along slice 6.

Fig. 3: Slices (indexed 1–6) using for setting of thresholds I_{out} , I_{in} . Gray points corresponds to the minima found by described algorithm, black points corresponds to the intersections of initial segmentation curve and given slices.

V. PARAMETER SETTING

In this Section we explain how the computational parameters for the segmentation of the left heart ventricle from MRI images are set up. To apply the scheme derived from (19), we have to specify the suitable values of the parameters in equation (11), such as the parameter λ , the standard deviation of Gauss function σ , the force parameter F , the advection parameter \mathcal{A} , the regularization parameter ε , the spatial step h , the time step τ and the stopping criterion (how many time iterations are needed to get the desired result).

The parameters are set-up with an agreement of the model requirements and are tuned by the practice and experience with the model and used image data. The approach presented here is applicable on wide set of image data. On the other hand, applying this approach to different image data types require additional tuning of the parameters. Consequently, each parameter have to be tailored to given set of image data types.

A. Parameters λ and σ

The parameters λ and σ are included in the edge detector g^0 defined in Section II. The parameter σ characterizes the variance of Gaussian smoothing kernel which is responsible for the presmoothing of the input images. Higher values of σ cause stronger reduction of noise. On the other hand, this type of presmoothing lowers the image gradient, i.e. blurs the image.

The sensitivity of the edge detector depends on value of the parameter λ . Very low values of λ decrease the efficiency of the edge detection. On the other hand, very high values of λ can cause the detection of spurious edges (i.e. noise, blood flow artifacts, etc.).

These two parameters are dependent each of other. Higher values of σ require higher values of λ and vice versa. In our algorithm, we set $\sigma = 2h$ and $\lambda = 0.1$.

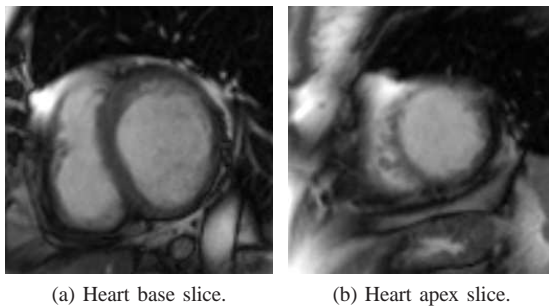


Fig. 4: Comparison of two heart slices (apex and base) of one patient.

B. Parameters F and \mathcal{A}

Correct left ventricle segmentation requires a detailed information on the image gradient. Some edges can be more significant than others. Nevertheless, the magnitude of image gradient is not a convenient measure of the image edge importance. As we can see in Figure 4 the heart wall between the left and right ventricle is much more visible in slices corresponding to the heart base (Figure 4a) than in slices belonging to the heart apex (Figure 4b). In other words, the image intensities and the magnitude of image gradient corresponding to the heart wall are significantly different. To unify these heart wall inhomogeneities we propose an

image dependent setting of the force parameter F and of the advection parameter \mathcal{A} .

We propose the external force parameter in the form

$$F(I^0) = \begin{cases} F_{\text{out}} & I^0 \leq I_{\text{out}}, \\ F_{\text{in}} \left(\frac{I^0 - I_{\text{out}}}{I_{\text{in}} - I_{\text{out}}} \right) & I_{\text{out}} < I^0 < I_{\text{in}}, \\ F_{\text{in}} & I^0 \geq I_{\text{in}}, \end{cases} \quad (33)$$

where F_{out} is the value of the force parameter for the picture elements outside the left ventricle and F_{in} is the value of the force parameter for the picture elements surely inside the left ventricle. For the picture elements surely outside the ventricle, the evolution curve should shrink. The value of F_{out} has to be negative. The value F_{in} has to be positive, as discussed in Section II-A.

Similarly we propose the advection term, namely

$$\mathcal{A}(I^0) = \begin{cases} \mathcal{A}_{\text{out}} & I^0 \leq I_{\text{out}}, \\ (\mathcal{A}_{\text{out}} - 1) \left(1 - \frac{I^0 - I_{\text{out}}}{I_{\text{in}} - I_{\text{out}}} \right) + 1 & I_{\text{out}} < I^0 < I_{\text{in}}, \\ 1 & I^0 \geq I_{\text{in}}, \end{cases} \quad (34)$$

where $\mathcal{A}_{\text{out}} > 1$. This means that the edges with lower intensity are more important than the edges with higher intensity. We use the following setting of the parameters: $F_{\text{in}} = 50$, $F_{\text{out}} = -10$, $\mathcal{A}_{\text{out}} = 2$.

C. Parameters ε , τ , h

The parameter ε provides the regularization of the denominator in (4). The convergence rate of the SOR method depends on this parameter – a lower value of ε slows down the convergence. The value $\varepsilon = 0.001$ is a suitable compromise.

The spatial step is given as $h = 1/(\max\{n_{x_1}, n_{x_2}\} - 1)$, the time step τ is given as $\tau = h/5$.

D. Stopping criterion

In this Section we deal with the problem of successful termination of the segmentation process. There are several possibilities to stop the process. The simplest criterion could be to stop the process after the prescribed N iterations are performed. This could be a good criterion for known input data only (we know the stopping time before we start the process). Better possibility is to use an automated stopping criterion. Typically the computation is stopped as soon as the following inequality holds (see [45]):

$$\frac{1}{M} \sum_{i,j} |u_{i,j}^k - u_{i,j}^{k-1}| \leq C\tau h^2, \quad (35)$$

where sum is over all grid points, $M = n_{x_1}n_{x_2}$ and C is a constant. As we can see from (35) this criterion is time and memory consuming because we have to store $u^k - 1$. At the same time (35) is too strict for our computation. It would be enough to consider the changes in the segmentation curve only (the zero level set of u).

In our algorithm we use the following automated stopping criterion

$$\sum_{i=1}^{N_0} |S(u^{k-i+1}) - S(u^{k-i})| = 0, \quad (36)$$

where $S(u^k)$ denotes the number of pixels inside the segmentation area, i.e. the number of grid points for which

$u_{i,j}^k \leq 0$. The criterion (36) claims that the process is stopped after k time iterations if $S(u^k) = S(u^{k-1}) = \dots = S(u^{k-N_0+1})$, i.e. the segmentation area (segmentation curve) stops changing. In our experience good results are achieved using $N_0 = 3$.

VI. SEGMENTATION RESULTS

Before discussing results of segmentation, we introduce the notion of the ejection fraction. The ejection fraction (EF) is the most widely used measurement of left ventricular systolic function providing important prognostic information of patients. In other words, EF is the fraction of blood pumped out from the ventricle and is used clinically to determine myocardial contractility representing the performance of the heart. EF is defined as $EF = (EDV - ESV)/EDV$, where EDV denotes the end-diastolic volume, which corresponds to maximal volume of the ventricle (end-diastolic phase) and ESV stands for the end-systolic volume which corresponds to minimal volume of the ventricle (end-systolic phase). In general, normal range is between 55% and 70% (see [1], Chap. 6).

The algorithm was tested on hundreds of images belonging to tens of patients¹. Here, we present the result of segmentation for 15 patients (denoted by *Patient01* – *Patient15*). In table II the estimation of EDV, ESV and EF are presented. We compare results of our algorithm (LS) with the Allen-Cahn approach and automatically (SA) and manually (SM) processed data using SEGMENT software available on [46]. In Figures 7 – 8 the graphs of LV volume during the heart period is shown. In each Figure we can see four graphs: the black solid line corresponds to the result obtained by our algorithm, the gray solid line denotes the Allen-Cahn approach and remaining lines corresponds to the results acquired by SEGMENT software – automatic segmentation is denoted by black dashed line whereas gray dashed line shows the manual segmentation.

The **SEGMENT** is a freely available software for cardiovascular image analysis. It can be used for the analysis of the MR data. The software provides an automated segmentation of the left ventricle as well as a manual and general object segmentation. The segmentation algorithm is based on the concept of deformable objects. The geometrical representation of an image object can be deformed under the internal deformation energy and the external potential energy field. The energy minimization is described by the Euler-Lagrange equations (see [47]).

As an example of the segmentation results we selected image data of two patients – *Patient03* and *Patient13*. The results of the segmentation can be seen in Figures 5 (*Patient03*) and 6 (*Patient13*). The images are depicted in EDV and ESV phase. The white line represents the segmented region. After the segmentation is done we can plot the time evolution of the ventricle volume for each patient. Corresponding graphs of left ventricle volume during one cardiac cycle are depicted in Figures 7 and 8.

As can be seen in Table II or in Figure 7, the *Patient03* has low EF (19.81%), whereas the *Patient13* has higher EF (63.68%) as shows Table II or Figure 8. Figures 5 and 6 show sufficient segmentation result both for *Patient03* with low

contractility of myocardium and for *Patient14* with higher contractility. In Figure 5 we can see that a border of a segmented area lies precisely at the heart wall including a “peninsula” (papillary muscle). The peninsula can be clearly seen in the second image in Figures 5a and 5b.

VII. DISCUSSION

Our algorithm uses adaptive choice of parameters F (33) and \mathcal{A} (34) which are crucial in obtaining satisfactory segmentation results. The dependence of the algorithm on the thresholds I_{in} and I_{out} could be limiting. Inoptimal settings of these thresholds can cause inaccurate segmentation results. Therefore it is important to apply a robust automatic threshold selection. On the other hand, in the case of LV segmentation the threshold selection described in Section IV seems to be a good compromise between robustness and simplicity. Indeed, the presented results in Section VI justify applicability of the used threshold choice.

In the level set approach to the image segmentation there are various choices of initial condition settings. The initial segmentation function is set as the signed distance function with the zero level set corresponding to the initial segmentation curve. A benefit of this approach lies in an easy manipulation with the segmentation curve. For shrinking or expanding the segmentation curve we add or subtract some positive constant. Figure 6 shows a certain inaccuracy in segmentation of the peninsula. In the first image in 6a and 6b we can see that the black small “island” (papillary muscle) inside the ventricle is incorporated into the segmented area adding error to the ventricle volume estimation. It could be caused by both low gradient on the “island” and the initial condition setting discussed in Section II-A. As the initial curve is set as the result of the previous segmentation, the “island” could lie inside the domain defined by the initial segmentation curve. Consequently, the “island” is already included inside the initial segmentation curve at the start of segmentation process and remains there during the segmentation process. This problem could be easily solved by putting the initial curve outside the papillary muscle. We can shrink the initial segmentation curve by adding a positive constant to the initial segmentation function.

We have performed computational studies and comparison measurements presented here both in graphical and numerical form. Comparison to other methods including the manual segmentation is presented in Section VI. The manually segmented data should be the most accurate method. On the other hand, the segmented data by two different experts could differ. Despite of that, we consider the comparison presented here as appropriate.

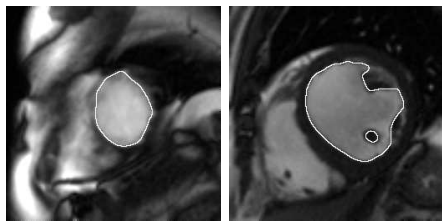
VIII. CONCLUSION

In the presented paper we discussed the adaptive segmentation algorithm based on the level set equation in the context of cardiac MRI data segmentation. The algorithm is based on the numerical scheme using the semi-implicit discretization in time and the co-volume method in space. We proposed a new advection and force parameter depending on the real cardiac MRI data². Moreover, the results were compared both to the other methods and to the manually segmented data.

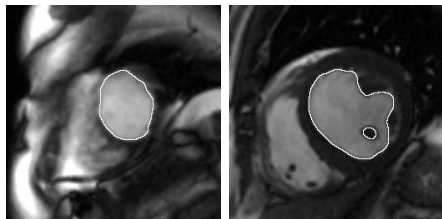
¹The data were provided by the Institute for Clinical and Experimental Medicine in Prague.

²IKEM Praha, <http://www.ikem.cz/www/en>

APPENDIX A
SEGMENTATION RESULTS – FIGURES AND TABLES

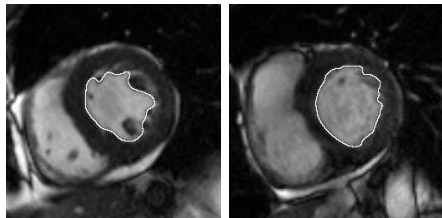


(a) Result of segmentation (end-diastole)

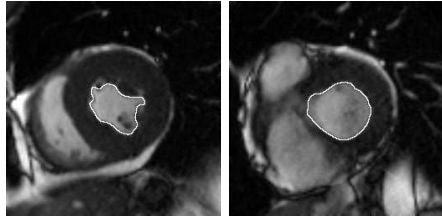


(b) Result of segmentation (end-systole)

Fig. 5: Patient03. Results for (a) EDV and (b) ESV using $h = 0.0039$, $\lambda = 1.0$, $\mathcal{A}_{out} = 2$, $F_{out} = -10$, $F_{in} = 50$.



(a) Result of segmentation (end-diastole)



(b) Result of segmentation (end-systole)

Fig. 6: Patient13. Results for (a) EDV and (b) ESV using $h = 0.0039$, $\lambda = 1.0$, $\mathcal{A}_{out} = 2$, $F_{out} = -10$, $F_{in} = 50$.

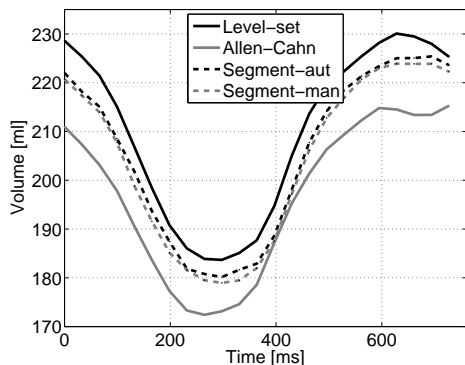


Fig. 7: Plot of ventricle volume vs time for Patient03.

REFERENCES

[1] J. Bogaert, S. Dymarkowski, A. Taylor, and V. Muthurangu, *Clinical Cardiac MRI*, ser. Medical radiology. Springer Berlin Heidelberg, 2012. [Online]. Available: <http://books.google.cz/books?id=Cuz4ayP8rZkC>

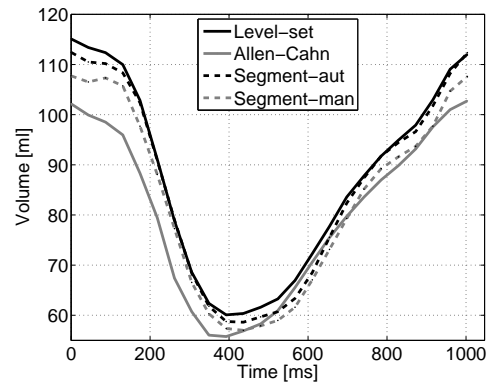


Fig. 8: Plots of ventricle volume vs time for Patient13.

[2] S. Corsaro, K. Mikula, A. Sarti, and F. Sgallari, “Semi-implicit co-volume method in 3D image segmentation,” *SIAM Journal on Scientific Computing*, vol. 28, no. 6, pp. 2248–2265, 2006.

[3] A. Handlovičová and K. Mikula, “Stability and consistency of the semi-implicit co-volume scheme for regularized mean curvature flow equation in level set formulation,” *Applications of Mathematics*, vol. 53, no. 2, pp. 105–129, 2008.

[4] K. Mikula, T. Preusser, and M. Rumpf, “Morphological image sequence processing,” *Computing and Visualization in Science*, vol. 6, no. 4, pp. 197–209, 2004.

[5] K. Mikula, A. Sarti, and F. Sgallari, “Co-volume level set method in subjective surface based medical image segmentation,” in *Handbook of Biomedical Image Analysis*. Springer, 2005, pp. 583–626.

[6] R. Máca, M. Beneš, and J. Tintěra, “Application of degenerate diffusion method in medical image processing,” *Journal of Math-for-Industry*, vol. 3, pp. 33–40, 2011.

[7] D. Cremers, M. Rousson, and R. Deriche, “A review of statistical approaches to level set segmentation: integrating color, texture, motion and shape,” *International journal of computer vision*, vol. 72, no. 2, pp. 195–215, 2007.

[8] M. Kass, A. Witkin, and D. Terzopoulos, “Snakes: Active contour models,” *International journal of computer vision*, vol. 1, no. 4, pp. 321–331, 1988.

[9] V. Caselles, R. Kimmel, and G. Sapiro, “Geodesic active contours,” *International journal of computer vision*, vol. 22, no. 1, pp. 61–79, 1997.

[10] T. F. Chan and L. A. Vese, “Active contours without edges,” *Image Processing, IEEE Transactions on*, vol. 10, no. 2, pp. 266–277, 2001.

[11] T. Goldstein, X. Bresson, and S. Osher, “Geometric applications of the split Bregman method: segmentation and surface reconstruction,” *Journal of Scientific Computing*, vol. 45, no. 1-3, pp. 272–293, 2010.

[12] J. Cheng, Y. Liu, R. Jia, and W. Guo, “A new active contour model for medical image analysis-wavelet vector flow,” *IAENG International Journal of Applied Mathematics*, vol. 36, pp. 33–37, 2007.

[13] C. Bandle, A. Brillard, G. Dziuk, and A. Schmidt, “Course on mean curvature flow,” *Manuscript 75p.*, 1994. [Online]. Available: <http://www.mathematik.uni-freiburg.de/IAM/homepages/alfred/>

[14] K. Deckelnick and G. Dziuk, “Mean curvature flow and related topics,” *Frontiers in Numerical Analysis: Durham 2002*, p. 63, 2003.

[15] L. C. Evans and J. Spruck, “Motion of level sets by mean curvature I,” *Journal of Differential Geometry*, vol. 33, pp. 381–635, 1991.

[16] S. Osher and R. Fedkiw, *Level set methods and dynamic implicit surfaces*. Springer Verlag, 2003, vol. 153.

[17] J. A. Sethian, *Level set methods and fast marching methods: evolving interfaces in computational geometry, fluid mechanics, computer vision, and materials science*. Cambridge university press, 1999, vol. 3.

[18] A. Delong, A. Osokin, H. N. Isack, and Y. Boykov, “Fast approximate energy minimization with label costs,” *International Journal of Computer Vision*, vol. 96, no. 1, pp. 1–27, 2012.

[19] D. Mumford and J. Shah, “Optimal approximations by piecewise smooth functions and associated variational problems,” *Communications on pure and applied mathematics*, vol. 42, no. 5, pp. 577–685, 1989.

[20] N. Paragios and R. Deriche, “Geodesic active regions: A new framework to deal with frame partition problems in computer vision,” *Journal of Visual Communication and Image Representation*, vol. 13, no. 1, pp. 249–268, 2002.

[21] K. Deshmukh and G. Shinde, “Adaptive color image segmentation

TABLE II: Estimated EF, EDV and ESV for Patient01 – Patient15 using level set algorithm (LS), Allen-Cahn approach (AC), automatical tools in program Segment (SA) and manual segmentation in program Segment (SM). **Bold (italic)** font shows the best (worst) fit with respect to the manual segmentation.

Patient		01		02		03		04		05		06		07		08	
Value		abs	e[%]	abs	e[%]												
EF [%]	LS	9.91	0.53	10.19	2.31	19.81	1.01	20.17	0.09	20.38	-2.12	22.80	1.05	24.15	0.16	24.66	0.20
	AC	10.34	0.96	7.76	-0.12	18.54	-0.26	19.91	-0.17	21.90	-0.60	22.83	1.08	21.64	-2.35	25.22	0.76
	SA	7.84	<i>-1.54</i>	7.24	-0.64	16.63	-2.17	20.07	-0.01	19.95	-2.55	21.32	-0.43	19.27	<i>-4.72</i>	22.36	-2.10
	SM	9.38	-	7.88	-	18.80	-	20.08	-	22.50	-	21.75	-	23.99	-	24.46	-
EDV [ml]	LS	297.90	0.87	171.12	2.23	295.34	-2.19	230.08	2.75	202.09	-1.97	225.54	-0.79	183.72	0.11	83.19	1.19
	AC	296.16	0.28	166.58	-0.48	286.57	-5.09	215.28	-3.86	186.31	-9.62	221.70	-2.48	183.97	0.25	81.75	-0.56
	SA	293.03	-0.78	177.72	6.18	290.12	-3.91	225.39	0.66	201.84	-2.09	239.02	5.14	184.19	0.37	80.67	-1.87
	SM	295.32	-	167.38	-	301.94	-	223.92	-	206.15	-	227.34	-	183.51	-	82.21	-
ESV [ml]	LS	268.39	0.29	153.68	-0.34	236.82	-3.40	183.67	2.63	160.91	0.72	174.12	-2.12	139.35	-0.10	62.68	0.93
	AC	265.54	-0.78	153.64	-0.36	233.45	-4.78	172.41	-3.66	145.50	-8.93	171.08	-3.83	144.15	3.34	61.13	-1.56
	SA	270.04	0.90	164.86	6.91	241.88	-1.34	180.15	0.66	161.58	1.14	188.07	5.72	148.70	6.60	62.63	0.85
	SM	267.62	-	154.20	-	245.16	-	178.96	-	159.76	-	177.89	-	139.49	-	62.10	-

Patient		09		10		11		12		13		14		15	
Value		abs	e[%]	abs	e[%]	abs	e[%]	abs	e[%]	abs	e[%]	abs	e[%]	abs	e[%]
EF [%]	LS	28.33	2.60	28.38	-0.36	42.69	-0.70	42.85	0.84	47.81	0.72	63.68	1.21	64.16	3.13
	AC	28.27	2.54	28.48	-0.26	36.73	-6.66	40.32	-1.69	45.74	-1.35	55.04	-7.43	60.05	-0.98
	SA	20.91	-4.82	27.30	-1.44	45.11	1.72	41.26	-0.75	47.85	0.76	62.86	0.39	60.66	-0.37
	SM	25.73	-	28.74	-	43.39	-	42.01	-	47.09	-	62.47	-	61.03	-
EDV [ml]	LS	147.19	-1.51	127.66	-1.58	75.46	2.14	173.40	13.32	115.11	6.85	90.53	6.74	99.42	-4.52
	AC	149.97	0.35	121.80	-6.10	72.84	-1.41	177.53	16.02	102.76	-4.61	87.75	3.47	94.28	-9.46
	SA	150.44	0.67	129.11	-0.46	72.81	-1.45	154.07	0.69	112.43	4.36	88.63	4.50	109.69	5.34
	SM	149.44	-	129.71	-	73.88	-	153.02	-	107.73	-	84.81	-	104.13	-
ESV [ml]	LS	105.49	-4.96	91.43	-1.08	43.24	3.37	99.10	11.69	60.08	5.40	32.88	3.30	35.63	-12.20
	AC	107.57	-3.08	87.11	-5.76	46.08	10.16	105.95	19.41	55.76	-2.18	39.46	23.97	37.67	-7.17
	SA	118.98	7.20	93.86	1.55	39.96	-4.47	90.50	1.99	58.63	2.86	32.91	3.39	43.16	6.36
	SM	110.99	-	92.43	-	41.83	-	88.73	-	57.00	-	31.83	-	40.58	-

using fuzzy min-max clustering.” *Engineering Letters*, vol. 13, no. 2, pp. 57–64, 2006.

[22] K. Mikula, *Numerical solution, analysis and application of geometrical nonlinear diffusion equations*. Publishing House of the Slovak University of Technology, Bratislava, 2006, no. 34.

[23] F. Cao, *Geometric curve evolution and image processing*. Springer Verlag, 2003, vol. 1805.

[24] G. Sapiro, *Geometric partial differential equations and image analysis*. Cambridge university press, 2006.

[25] M. Beneš, “Mathematical analysis of phase-field equations with numerically efficient coupling terms,” *Interfaces and Free Boundaries*, vol. 3, no. 2, pp. 201–212, 2001.

[26] M. Beneš, V. Chalupský, and K. Mikula, “Geometrical image segmentation by the Allen-Cahn equation,” *Applied Numerical Mathematics*, vol. 51, no. 2, pp. 187–205, 2004.

[27] S. M. Allen and J. W. Cahn, “A microscopic theory for antiphase boundary motion and its application to antiphase domain coarsening,” *Acta Metallurgica*, vol. 27, no. 6, pp. 1085–1095, 1979.

[28] R. Chabiniok and J. Tintěra, “Cardiac MRI data segmentation using the partial differential equation of Allen-Cahn type,” in *Proceedings of the Czech-Japanese Seminar in Applied Mathematics*, M. Beneš, M. Kimura, and T. Nakaki, Eds., vol. 6. Faculty of Mathematics, Kyushu University Fukuoka, 2006.

[29] R. Chabiniok, R. Máca, M. Beneš, and J. Tintěra, “Segmentation of MRI data by means of nonlinear diffusion,” *Kybernetika*, vol. 49, no. 2, pp. 301–318, 2013.

[30] Y. Boykov and V. Kolmogorov, “An experimental comparison of min-cut/max-flow algorithms for energy minimization in vision,” *Pattern Analysis and Machine Intelligence, IEEE Transactions on*, vol. 26, no. 9, pp. 1124–1137, 2004.

[31] Y. Y. Boykov and M.-P. Jolly, “Interactive graph cuts for optimal boundary & region segmentation of objects in ND images,” in *Computer Vision, 2001. ICCV 2001. Proceedings. Eighth IEEE International Conference on*, vol. 1. IEEE, 2001, pp. 105–112.

[32] A. Delong and Y. Boykov, “Globally optimal segmentation of multi-region objects,” in *Computer Vision, 2009 IEEE 12th International Conference on*. IEEE, 2009, pp. 285–292.

[33] F. R. Schmidt and Y. Boykov, “Hausdorff distance constraint for multi-surface segmentation,” in *Computer Vision–ECCV 2012*. Springer, 2012, pp. 598–611.

[34] A. Besbes, N. Komodakis, B. Glocker, G. Tziritas, and N. Paragios, “4D ventricular segmentation and wall motion estimation using efficient discrete optimization,” in *Proceedings of the 3rd international conference on Advances in visual computing–Volume Part I*. Springer-Verlag, 2007, pp. 189–198.

[35] M. Lynch, O. Ghita, and P. F. Whelan, “Segmentation of the left ventricle of the heart in 3-D+t MRI data using an optimized nonrigid temporal model,” *Medical Imaging, IEEE Transactions on*, vol. 27, no. 2, pp. 195–203, 2008.

[36] J. Montagnat and H. Delingette, “4D deformable models with temporal constraints: application to 4D cardiac image segmentation,” *Medical Image Analysis*, vol. 9, no. 1, pp. 87–100, 2005.

[37] M. G. Crandall, H. Ishii, and P.-L. Lions, “Users guide to viscosity solutions of second order partial differential equations,” *Bulletin of the American Mathematical Society*, vol. 27, no. 1, pp. 1–67, 1992.

[38] M.-P. Jolly, “Automatic segmentation of the left ventricle in cardiac MR and CT images,” *International Journal of Computer Vision*, vol. 70, no. 2, pp. 151–163, 2006.

[39] N. Paragios, “Variational methods and partial differential equations in cardiac image analysis,” in *Biomedical Imaging: Nano to Macro, 2004. IEEE International Symposium on*. IEEE, 2004, pp. 17–20.

[40] M. Rousson and N. Paragios, “Prior knowledge, level set representations & visual grouping,” *International Journal of Computer Vision*, vol. 76, no. 3, pp. 231–243, 2008.

[41] P. Perona and J. Malik, “Scale-space and edge detection using anisotropic diffusion,” *Pattern Analysis and Machine Intelligence, IEEE Transactions on*, vol. 12, no. 7, pp. 629–639, 1990.

[42] H. Zhao, “A fast sweeping method for eikonal equations,” *Mathematics of computation*, vol. 74, no. 250, pp. 603–627, 2005.

[43] M. Beneš, M. Kimura, P. Pauš, D. Ševčovič, T. Tsujikawa, and S. Yazaki, “Application of a curvature adjusted method in image segmentation,” *Bulletin of the Institute of Mathematics, Academia Sinica (New Series)*, pp. 509–523, 2008.

[44] A. Handlovičová, K. Mikula, and A. Sarti, “Numerical solution of parabolic equations related to level set formulation of mean curvature flow,” *Computing and visualization in Science*, vol. 1, no. 3, pp. 179–182, 1998.

[45] H.-K. Zhao, T. Chan, B. Merriman, and S. Osher, “A variational level set approach to multiphase motion,” *Journal of computational physics*, vol. 127, no. 1, pp. 179–195, 1996.

[46] E. Heiberg, J. Sjögren, M. Ugander, M. Carlsson, H. Engblom, and H. Arheden, “Design and validation of Segment-freely available software for cardiovascular image analysis,” *BMC medical imaging*, vol. 10, no. 1, p. 1, 2010.

[47] E. Heiberg, L. Wigstrom, M. Carlsson, A. Bolger, and M. Karlsson, “Time resolved three-dimensional automated segmentation of the left ventricle,” in *Computers in Cardiology, 2005. IEEE, 2005*, pp. 599–602.